

Short-time variability study of BHXB using a state-space model

Masato Noda,^{a,*} Makoto Uemura,^a Tomoki Omama^b and Masahiro Tsujimoto^b

^a*Hiroshima University*

Kagamiyama 1-3-1, Higashi-Hiroshima, Japan

^b*ISAS/JAXA*

3-1-1 Yoshinodai, Chuo-ku, Sagamiara, Kanagawa 252-5210, Japan

E-mail: noda@astro.hiroshima-u.ac.jp

Black hole X-ray binaries (BHXB) exhibit rapid variability across different energy bands, reflecting the complex interplay of multiple emission components such as accretion disks and coronas. Traditionally, spectral and temporal analyses have been conducted separately, making it difficult to disentangle the variability and causal relationships among these components. Omama (2024) introduced a state-space modeling framework for spectral-timing data of BHXB, allowing for the decomposition of light curves into distinct emission sources. Applying this method to MAXI J1820+070 in the low-hard state, Omama (2024) suggested a causal propagation of variability from the accretion disk to the Compton cloud, and subsequently to the soft excess. In this study, we applied the same model to an independent dataset of MAXI J1820+070 obtained on the same day to evaluate its robustness. Using six datasets, we confirmed consistency in power spectra, time lags, and power contributions of each component. We further extended our analysis to five additional epochs during the low-hard state between March and July 2018. The variability propagation pattern remained unchanged, but we observed a decrease in low-frequency power of both the accretion disk and Compton cloud. Notably, the break frequency of the Compton cloud increased over time, whereas the disk did not show such evolution, implying a gradual contraction of the Compton cloud region.

The 87th Fujihara Seminar: The 50th Anniversary Workshop of the Disk Instability Model in Compact Binary Stars

Tomakomai, Hokkaido, Japan

22nd to 26th (September 2025)

*Speaker

1. Introduction

Black hole X-ray binaries (BHXBs) show rapid variability on timescales down to milliseconds across energy bands [1, 2]. Conventional spectral and timing analyses have been performed separately, which makes it difficult to interpret the causal relationships among physical emission components such as accretion disks, coronas, and soft-excess emission.

Recently, Omama (2024) [3] introduced a linear Gaussian state-space model to simultaneously analyze the spectral and temporal behavior of MAXI J1820+070, one of the brightest transient BHXBs discovered in 2018. The model decomposes the observed light curves into latent components corresponding to distinct emission sources and captures their causal variability propagation. Applying this model, Omama (2024) revealed that the variability originates from the accretion disk, propagates through the Comptonized corona, and finally reaches the soft-excess component. These results provided a unified interpretation of spectral-timing variability in BHXBs.

In this work, we extend the state-space modeling framework to multiple epochs of MAXI J1820+070 during its 2018 low-hard state [4], aiming to test the robustness and temporal evolution of the inferred causal structure. By analyzing multiple epochs that span different stages of the outburst, we investigate whether the variability propagation pattern and physical coupling between the emission components remain stable or evolve over time.

2. Methods

2.1 Observation Data and Epochs

We used the *NICER* X-ray observations of MAXI J1820+070 obtained during its 2018 outburst. To ensure consistency with Omama (2024), we first analyzed the same epoch as in the original study to verify reproducibility. We then extended the analysis to four additional observational epochs, covering the early to late phases of the low-hard state, in order to investigate the temporal evolution of the variability properties. Table 1 summarizes the observation log used in this study. We selected the epoch used in Omama (2024) and additional epochs spaced by about one month; for June we chose an observation with sufficient exposure to enable the same analysis configuration. For each epoch, we extracted approximately five light-curve datasets with a time resolution of 0.1 s and a duration of 50 s each. Thus, a dataset includes 500 time-series points.

Omama (2024) performed a spectral analysis, and proposed three spectral components, that is, the power-law, the disk-blackbody (hereafter, disk-bb), and the soft-excess components. We represent these three components as elements of the latent variable vector,

$$\mathbf{x}_n = [x_n(1) \ x_n(2) \ x_n(3)]^T, \quad (1)$$

where $x_n(1)$, $x_n(2)$, and $x_n(3)$ correspond to the power-law, disk-bb, and soft-excess components, respectively. Based on this spectral analysis, we generate light curves of five energy bands: 0.5–1.0 keV, 1.0–1.5 keV, 1.5–2.0 keV, 2.0–5.0 keV, and 5.0–10.0 keV. The power-law component only contributes to the hardest band (5.0–10.0 keV), while both the power-law and disk-bb components contribute to the 2.0–5.0 keV band. All components can contribute to the other bands. In the current study, we also apply this configuration used in Omama (2024) to other datasets.

Table 1: NICER observation log of MAXI J1820+070 used in this study.

Obs ID	Date (UT)	Start Time (UT)	Exposure (s)
1200120106	2018/03/21	09:15:20	5437.54
1200120113	2018/03/28	06:45:20	2020.30
1200120133	2018/04/21	00:51:40	4729.00
1200120156	2018/05/22	05:36:12	6683.98
1200120157	2018/05/23	04:50:04	5430.09
1200120176	2018/06/11	02:52:34	5963.00

2.2 State-space modeling framework

State equation:

In this study, the variability of the three latent emission components is modeled using a second-order vector autoregressive model, VAR(2). The temporal evolution of the latent variable vector is given by:

$$\mathbf{x}_n = A_1 \mathbf{x}_{n-1} + A_2 \mathbf{x}_{n-2} + \mathbf{b} + \mathbf{v}_n, \quad (2)$$

where A_1 and A_2 are the VAR matrices and \mathbf{v}_n represents the state noise. $\mathbf{b} = (b_1, b_2, b_3)$ is an intercept term. To express the VAR(2) process in the standard companion form, the latent variable vector is augmented as follows:

$$\begin{bmatrix} \mathbf{x}_n \\ \mathbf{x}_{n-1} \end{bmatrix} = \begin{bmatrix} A_1 & A_2 \\ I & 0 \end{bmatrix} \begin{bmatrix} \mathbf{x}_{n-1} \\ \mathbf{x}_{n-2} \end{bmatrix} + \begin{bmatrix} \mathbf{b} \\ 0 \end{bmatrix} + \begin{bmatrix} \mathbf{v}_n \\ 0 \end{bmatrix}, \quad (3)$$

$$A_i = \begin{bmatrix} a_{i,11} & a_{i,12} & a_{i,13} \\ a_{i,21} & a_{i,22} & a_{i,23} \\ a_{i,31} & a_{i,32} & a_{i,33} \end{bmatrix} \quad (i = 1, 2). \quad (4)$$

The state noise is assumed to follow:

$$\mathbf{v}_n \sim \mathcal{N}(0, Q), \quad Q = I. \quad (5)$$

Observation equation:

The relationship between the latent variable vector \mathbf{x}_n and the observation variable vector \mathbf{y}_n is given by:

$$\mathbf{y}_n = H_1 \mathbf{x}_n + \mathbf{w}_n, \quad (6)$$

where the observation variable vector \mathbf{y}_n is defined as

$$\mathbf{y}_n = [y_n(1) \ y_n(2) \ y_n(3) \ y_n(4) \ y_n(5)]^T. \quad (7)$$

$y_n(1) \cdots y_n(5)$ represent the light curves from the hardest (5.0–10.0 keV) to softest (0.5–1.0 keV) energy bands, respectively. The observation matrix H_1 is written as

$$H_1 = \begin{bmatrix} h_4 & 0 & 0 \\ h_6 & h_5 & 0 \\ h_3 & h_2 & h_1 \\ h_7 & h_8 & h_9 \\ h_{10} & h_{11} & h_{12} \end{bmatrix}. \quad (8)$$

The observation noise is assumed to follow

$$\mathbf{w}_n \sim \mathcal{N}(0, L_R L_R^\top), \quad (9)$$

where the lower-triangular matrix L_R is written as

$$L_R = \begin{bmatrix} r_6 & 0 & 0 & 0 & 0 \\ r_{11} & r_{12} & 0 & 0 & 0 \\ r_{15} & r_{14} & r_{13} & 0 & 0 \\ r_{10} & r_9 & r_8 & r_7 & 0 \\ r_5 & r_4 & r_3 & r_2 & r_1 \end{bmatrix}. \quad (10)$$

The subscripts in H_1 and L_R follow the parameter ordering of Omama (2024). This state-space formulation enables joint spectral–temporal analysis by providing a unified representation from which power spectra, cross-correlation functions, and Granger causalities can be analytically derived. Parameter estimation was performed using Markov Chain Monte Carlo (MCMC) sampling with 2000 iterations.

2.3 Power spectrum, cross-correlation function, and Granger causality

From the VAR coefficients in A_1 and A_2 , we reconstructed the latent time series and derived the corresponding power spectra, cross-correlation functions, and Granger causalities.

Power spectrum:

In the VAR modeling framework, the cross-spectrum matrix $P(f)$ is the fundamental quantity from which the individual component power spectra are derived. The power spectrum $P_{ii}(f)$ of the i -th component is given by the i -th diagonal element of $P(f)$. The cross-spectrum matrix is defined as follows:

$$P(f) = A(f)^{-1} W \left(A(f)^{-1} \right)^*, \quad (11)$$

where W denotes the white noise variance–covariance matrix. The frequency-domain coefficient matrix $A(f)$ is defined as follows:

$$A_{jk}(f) = \sum_{m=0}^M a_m(j, k) e^{-2\pi i m f}, \quad (12)$$

where $a_m(j, k)$ denotes the (j, k) element of the VAR coefficient matrix A_m . For the $m = 0$ term, the coefficients are defined as follows:

$$a_0(j, k) = \begin{cases} -1, & j = k, \\ 0, & j \neq k. \end{cases} \quad (13)$$

In the current model defined in the last section, $M = 2$ and $W = Q$.

Cross-correlation function:

In the VAR framework, the time-lagged correlation structure of the latent components is characterized through the cross-covariance matrices $\{C_k\}$, where C_k denotes the covariance matrix at time lag k :

$$C_k = \text{Cov}(\mathbf{x}_{n+k}, \mathbf{x}_n). \quad (14)$$

For a VAR(M) process, the cross-covariance matrices satisfy the Yule–Walker equations:

$$C_0 = \sum_{j=1}^M A_j C_{-j} + W, \quad (15)$$

$$C_k = \sum_{j=1}^M A_j C_{k-j}, \quad k = 1, 2, \dots \quad (16)$$

The matrices C_{-j} denote the backward-lag covariances and satisfy

$$C_{-j} = C_j^T. \quad (17)$$

The normalized cross-correlation function is then obtained as

$$R_k(i, j) = \frac{C_k(i, j)}{\sqrt{C_0(i, i) C_0(j, j)}}, \quad (18)$$

which measures the correlation between components i and j at lag k . In the current model (VAR(2) with three latent components), these equations reduce to $M = 2$, A_1 and A_2 for the coefficient matrices, and $W = Q$ for the process noise covariance.

Granger causality:

To evaluate the directional influence between the latent emission components, we computed the Granger causality using the F -statistic. In this framework, Granger causality tests whether the past values of one component provide statistically significant predictive information for another. For each ordered pair of components, we compared two VAR models: (i) a restricted model that excludes the candidate causal component, and (ii) an unrestricted model that includes it. The test statistic is defined as follows:

$$F = \frac{(SSR_r - SSR_{ur})/q}{SSR_{ur}/(T - k)}, \quad (19)$$

where SSR_r and SSR_{ur} represent the residual sums of squares of the restricted and unrestricted models, respectively. Here, q , T , and k correspond to the number of excluded coefficients, the number of usable data points, and the number of free parameters in the unrestricted model. In the current model with VAR(2), $q = 2$, $T = 500 - 2$, and $k = 7$, including the intercept term. A larger value of F indicates a stronger causal influence from the candidate component to the target component. In this study, the F -statistic was computed for each epoch to evaluate how the causal coupling between components changes across epochs.

3. Results

3.1 Power Spectrum

Figure 1 shows the power spectrum of the three emission components—power-law, disk-bb, and soft-excess components—at the five epochs. The red curves correspond to the epoch analyzed in Omama (2024), where the power spectrum shows a flat shape at low frequencies with clear break frequencies at approximately 0.1 Hz for the power-law component, 0.3 Hz for the disk-bb component, and 0.03 Hz for the soft-excess component, followed by a steep decline toward higher

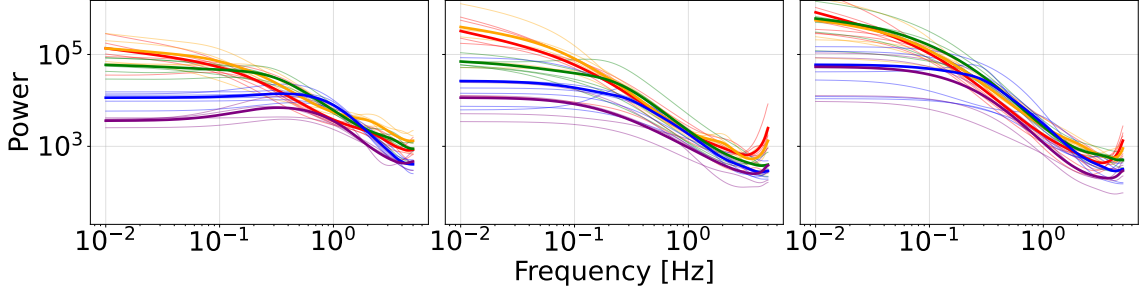


Figure 1: Power spectra of three radiation components across five epochs. From left to right, the panels show the power-law component, the disk-bb component, and the soft-excess component. Color coding corresponds to the observation date in 2018: red – March 21; orange – March 28; green – April 21; blue – May 22–23; purple – June 11. Thin lines show the power spectra estimated from individual 50-s datasets, while thick lines represent the mean spectrum for each epoch.

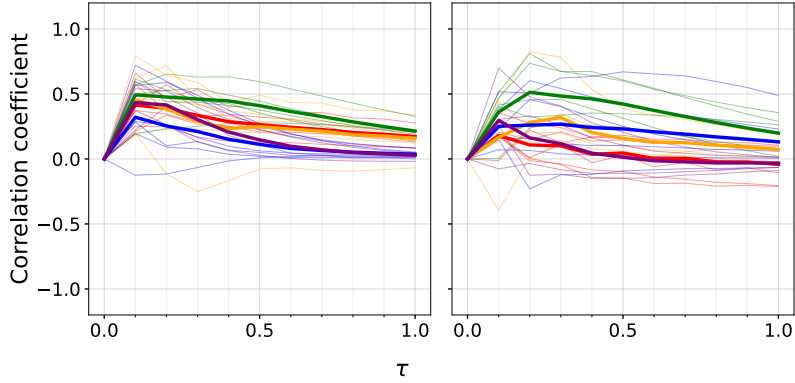


Figure 2: Cross-correlation functions (CCF) between the emission components across five epochs. Color coding and the distinction between thin (individual datasets) and thick (epoch-mean) lines follow the same convention as in Figure 1. Left: CCF between the disk-bb and power-law components. Right: CCF between the disk-bb and soft-excess components. The horizontal axis represents the time lag τ (s), and the vertical axis represents the correlation coefficient.

frequencies. This behavior is consistent with Omama (2024), demonstrating the reproducibility of this method.

In the low-frequency range, the power gradually decreased over time in all components. In contrast, at higher frequencies, the power-law component exhibited a modest increase in variability amplitude over time. Moreover, the break frequency of the power-law component shifted toward higher frequencies, whereas the disk-bb component showed no clear sign of such change. This spectral evolution suggests that the characteristic variability timescale shortened in the region emitting the power-law component.

While weak QPO-like features are occasionally visible in the power spectra of individual 50-s segments, such signals are not consistently detected across all segments. As a result, the QPO signature is diluted when averaging the power spectra over each epoch.

3.2 Cross-correlation function and time lag between components

Figure 2 shows the cross-correlation functions (CCF) between the components. The CCF of the disk-bb component with respect to the power-law component (left) shows a time lag at 0.1 s in

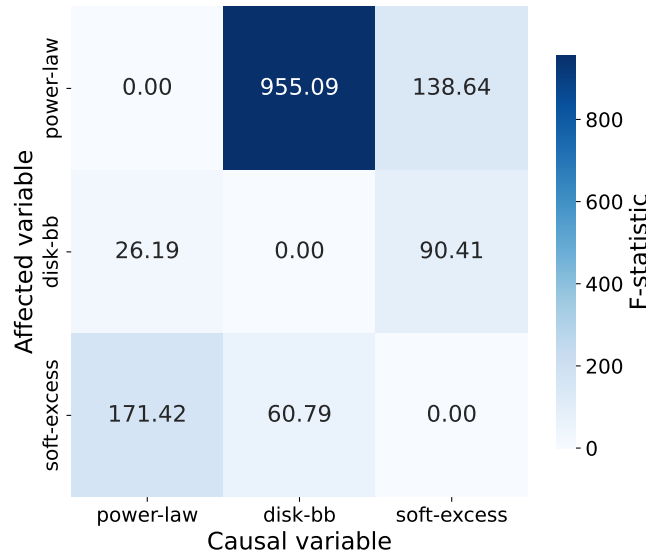


Figure 3: Heatmap of Granger causality for the dataset analyzed in Omama (2024). The horizontal and vertical axes correspond to the causal and affected components, respectively. The color intensity represents the strength of causality (F-statistic), with darker colors indicating stronger directional causality.

all five epochs. Since the time lag is evaluated with a resolution of 0.1 s, smaller variations may exist but cannot be resolved in the present analysis. The CCF of the disk-bb component with respect to the soft-excess component (right) shows a time lag at 0.1–0.2 s. These features confirm that the causal propagation path identified by Omama (2024) is robust and persists across multiple epochs.

3.3 Granger Causality

We next examined the causal relationships between the emission components using the Granger causality metric. Figure 3 presents a heatmap of causality strengths for the same dataset as analyzed by Omama (2024), confirming a strong causal influence from the disk-bb component to the power-law component.

We calculated the Granger causality to the data of the other epochs. Figure 4 shows the temporal evolution of the Granger causality. This was obtained by repeating the calculation shown in Figure 3 for each 50-second dataset and then taking the median value for each day. As can be seen in the figure, the overall causality strength gradually weakened with time. This weakening trend is particularly clear for the causality from the disk-bb to the power-law component. It indicates a reduction in the coupling between the disk and corona during the later stages of the low-hard state.

4. Discussion and Conclusion

Using state-space modeling with observational data from the same epoch as Omama (2024), the power spectra of the three emission components—power-law, disk-bb, and soft-excess components—exhibited flat shapes at low frequencies, with clear break frequencies of approximately 0.1, 0.3, and 0.03 Hz, respectively, followed by steep declines toward higher frequencies. The cross-correlation functions revealed stable time lags of about 0.1 s from the disk-bb to the power-law component and 0.1–0.2 s from the power-law to the soft-excess component, indicating a consistent

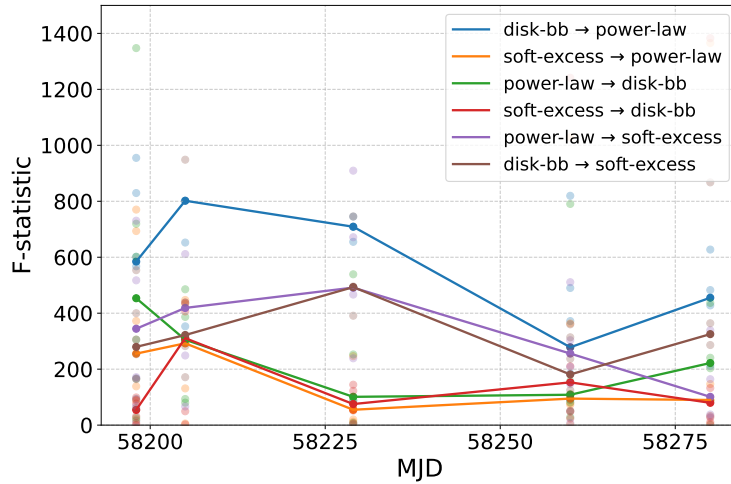


Figure 4: Temporal evolution of Granger causality across five epochs. The horizontal axis represents the epoch, and the vertical axis represents the median F-statistic value for Granger causality between each radiative component. Higher F-statistic values indicate stronger coupling.

propagation sequence among the components. These results are in good agreement with those reported by Omama (2024), confirming the reproducibility of the method and robustness of the inferred variability structure. Furthermore, by introducing Granger causality analysis, we quantitatively verified that the correlations identified by the cross-correlation functions represent causal relationships, reinforcing the interpretation of variability propagation within the disk-corona system.

In addition, we extend the analysis to five epochs throughout the low-hard state. Our result suggests that the corona—responsible for the power-law emission—gradually contracts and moves closer to the black hole over time. As a result, the emitting region may shift from outer to inner area, leading to the enhanced high-frequency variability. The lack of the enhanced high-frequency variability in the disk-bb and soft-excess components is possibly related to the decreasing causality, as shown in Figure 4. These findings demonstrate that the method proposed by Omama (2024) possesses high reproducibility and stability, and that it serves as a unique approach capable of extracting causal relationships among the radiative components.

References

- [1] M. Oda, K. Takagishi, M. Matsuoka, S. Miyamoto and Y. Ogawara, *Millisecond X-Ray Pulses from Cyg X-1*, *Publ. Astron. Soc. Japan* **26** (1974) 303.
- [2] R.A. Remillard and J.E. McClintock, *X-Ray Properties of Black-Hole Binaries*, *Annu. Rev. Astron. Astrophys.* **44** (2006) 49 [astro-ph/0606352].
- [3] T. Omama, *Joint Analysis of X-ray Spectral and Timing using the State-Space Model: Application for the Black Hole Binary MAXI J1820+070*, Ph.D. thesis, The Graduate University for Advanced Studies, 2024.
- [4] M. Shidatsu, S. Nakahira, K.L. Murata, R. Adachi, N. Kawai, Y. Ueda et al., *X-Ray and Optical Monitoring of State Transitions in MAXI J1820+070*, *Astrophys. J.* **874** (2019) 183 [1903.01686].